A new dynamical modeling of the WASP-47 system with CHEOPS observations

Nascimbeni, V.; Borsato, L.; Zingales, T.; Piotto, G.; Pagano, I.; Beck, M.; ... ; Wolter, D.

Astronomy & Astrophysics

A new dynamical modeling of the WASP-47 system with CHEOPS observations[*]

V. Nascimbeni[1] , L. Borsato[1], T. Zingales[2,1], G. Piotto[2,1], I. Pagano[3], M. Beck[4], C. Broeg[5,6], D. Ehrenreich[4,7], S. Hoyer[8], F. Z. Majidi[2,1], V. Granata[9,1], S. G. Sousa[10], T. G. Wilson[11], V. Van Grootel[12], A. Bonfanti[13], S. Salmon[4], A. J. Mustill[14,52], L. Delrez[15,12], Y. Alibert[5], R. Alonso[16,17], G. Anglada[18,19], T. Bárczy[20], D. Barrado[21], S. C. C. Barros[10,22], W. Baumjohann[13], T. Beck[5], W. Benz[5,6], M. Bergomi[1], N. Billot[4], X. Bonfils[23], A. Brandeker[24], J. Cabrera[25], S. Charnoz[26], A. Collier Cameron[11], Sz. Csizmadia[25], P. E. Cubillos[27,13], M. B. Davies[28], M. Deleuil[8], A. Deline[4], O. D. S. Demangeon[10,22], B.-O. Demory[6,5], A. Erikson[25], A. Fortier[5,6], L. Fossati[13], M. Fridlund[29,30], D. Gandolfi[31], M. Gillon[15], M. Güdel[32], K. G. Isaak[33], L. L. Kiss[34,35], J. Laskar[36], A. Lecavelier des Etangs[37], M. Lendl[4], C. Lovis[4], R. Luque[38,39], D. Magrin[1], P. F. L. Maxted[40], C. Mordasini[6], G. Olofsson[24], R. Ottensamer[41], E. Pallé[16], G. Peter[42], D. Piazza[5], D. Pollacco[43], D. Queloz[44,45], R. Ragazzoni[1,2], N. Rando[46], F. Ratti[46], H. Rauer[25,47,48], I. Ribas[18,19], N. C. Santos[10,22], G. Scandariato[3], D. Ségransan[4], A. E. Simon[5], A. M. S. Smith[25], M. Steinberger[13], M. Steller[13], Gy. M. Szabó[49,50], N. Thomas[5], S. Udry[4], J. Venturini[4], N. A. Walton[51], and D. Wolter[25]

(Affiliations can be found after the references)

ABSTRACT

Among the hundreds of known hot Jupiters (HJs), only five have been found to have companions on short-period orbits. Within this rare class of multiple planetary systems, the architecture of WASP-47 is unique, hosting an HJ (planet-b) with both an inner and an outer sub-Neptunian mass companion (-e and -d, respectively) as well as an additional non-transiting, long-period giant (-c). The small period ratio between planets -b and -d boosts the transit time variation (TTV) signal, making it possible to reliably measure the masses of these planets in synergy with the radial velocity (RV) technique. In this paper, we present new space- and ground-based photometric data of WASP-47b and WASP-47-d, including 11 unpublished light curves from the ESA mission CHaracterising ExOPlanet Satellite (CHEOPS). We analyzed the light curves in a homogeneous way together with all the publicly available data to carry out a global N-body dynamical modeling of the TTV and RV signals. We retrieved, among other parameters, a mass and density for planet -d of $M_{\rm d} = 15.5 \pm 0.8\ M_\oplus$ and $\rho_{\rm d} = 1.69 \pm 0.22$ g cm^{-3}, which is in good agreement with the literature and consistent with a Neptune-like composition. For the inner planet (-e), we found a mass and density of $M_{\rm e} = 9.0 \pm 0.5\ M_\oplus$ and $\rho_{\rm e} = 8.1 \pm 0.5$ g cm^{-3}, suggesting an Earth-like composition close to other ultra-hot planets at similar irradiation levels. Though this result is in agreement with previous RV plus TTV studies, it is not in agreement with the most recent RV analysis (at 2.8σ), which yielded a lower density compatible with a pure silicate composition. This discrepancy highlights the still unresolved issue of suspected systematic offsets between RV and TTV measurements. In this paper, we also significantly improve the orbital ephemerides of all transiting planets, which will be crucial for any future follow-up.

Key words. techniques: photometric – planets and satellites: detection – planets and satellites: general

1. Introduction

Hot Jupiters (HJs), that is, giant, gaseous planets ($0.3 \lesssim M_{\rm p} \lesssim 13\ M_{\rm jup}$) orbiting their host stars on very short orbits ($P \lesssim 10$ days), have been the subject of many "firsts" in the history of exoplanetary research, as the first planet discovered around a solar-type star (51 Peg b; Mayor & Queloz 1995) is an HJ and the first reported transiting planet (HD 209458 b; Charbonneau et al. 2000; Henry et al. 2000), which is also the first planet where an atmospheric feature has been detected (Charbonneau et al. 2002), is an HJ. Although 479 HJs have been discovered so far by various techniques[1], albeit mostly by combining transit photometry and radial velocity (RV) measurements,

many key questions are still unanswered about their formation, migration, and successive evolution (Dawson & Johnson 2018; Fortney et al. 2021).

Hundreds of multiple planetary systems have been detected with space-based missions such as Convection, Rotation and planetary Transits (CoRoT; Auvergne et al. 2009), Kepler/K2 (Borucki et al. 2010; Ricker et al. 2015), and the Transiting Exoplanet Survey Satellite (TESS; Ricker et al. 2015). These systems show great diversity in their architecture, with planets spanning the full range of planetary masses and being arranged in very different dynamical configurations. However, HJs have been known for a long time to be preferentially lonely when compared to other classes (Latham et al. 2011; Huang et al. 2016; Steffen et al. 2012), and almost all their known companions are long-period massive planets at $P \gtrsim 200$ days detected through either modulation or long-term trends in their RVs (Knutson et al. 2014). The rarity of HJ companions with inner or short-period orbits

---

[*] This article uses data from CHEOPS programs `CH_PR100017` and `CH_PR100025`. The individual data sets are listed in Table A.4.
[1] Source: NASA Exoplanet Archive. `https://exoplanetarchive.ipac.caltech.edu/`

Table 1. Mass measurements of the WASP-47 planets published in the literature.

Reference	$M_e/M_\oplus$	$M_b/M_\oplus$	$M_d/M_\oplus$	$M_c \sin i/M_\oplus$	Method
Hellier et al. (2012)	–	364 ± 16	–	–	RV
Neveu-VanMalle et al. (2016)	–	360 ± 19	–	396 ± 70	RV
Dai et al. (2015)	12.2 ± 3.7	370 ± 29	$10.4 \pm 8.4^{(\dagger)}$	–	RV
Becker et al. (2015)	$< 22^{(\ddagger)}$	341^{+73}_{-55}	15 ± 7	–	RV+TTV
Almenara et al. (2016)	$9.1^{+1.8}_{-2.9}$	364 ± 8	15.7 ± 1.1	361^{+80}_{-54}	RV+TTV[¶]
Weiss et al. (2017)	9.1 ± 1.0	358 ± 12	13.6 ± 2.0	416 ± 16	RV+TTV
Sinukoff et al. (2017)	9.1 ± 1.2	356 ± 12	12.7 ± 2.7	411 ± 18	RV
Vanderburg et al. (2017)	6.8 ± 0.7	363 ± 7	13.1 ± 1.5	398 ± 9	RV[§]
Bryant & Bayliss (2022)	6.8 ± 0.6	364 ± 7	14.2 ± 1.3	399 ± 9	RV[§]
This work (see also Table 4)	9.0 ± 0.5	374 ± 17	15.5 ± 0.8	447 ± 20	RV+TTV

Notes. [†]"Detected weakly if at all" (Dai et al. 2015). [‡]Upper limit at 95% confidence (Becker et al. 2015). [§]The errors on M_b and M_c are dominated by the relative uncertainty on the stellar mass $M_\star$ (see Sect. 4). [¶]Photodynamical approach.

has been confirmed by a recent global analysis of TESS photometry by Hord et al. (2021). There are only a handful of notable examples of HJs with nearby companions: WASP-47, the subject of this paper (see below), Kepler-730 (Zhu et al. 2018; Cañas et al. 2019), TOI-1130 (Huang et al. 2020), WASP-132 (Hord et al. 2022), and the most recently reported TOI-2000 (Sha et al. 2022). Together, these five planets represent less than 1% of the known HJs[2]. Notably, WASP-47 is unique among the mentioned systems for showing clear transit time variations (TTVs), allowing researchers to jointly exploit TTVs and RVs to measure the planetary masses and other orbital parameters in a much more reliable way than using the two techniques separately (Malavolta et al. 2017).

WASP-47 has been dubbed "the gift that keeps on giving" (Kane et al. 2020) due to the many layers of scientific investigation it has stimulated. The first member of this planetary system, HJ WASP-47b[3] (1.14 ± 0.02 M_{jup}, 1.127 ± 0.013 R_{jup}, $P \simeq 4.159$ days) was discovered by Hellier et al. (2012) from ground-based photometric data (SuperWASP). A few years later, WASP-47 was observed by K2 during its Campaign 3, enabling the detection of two additional companions (Becker et al. 2015): WASP-47e (6.8 ± 0.7 $M_\oplus$, 1.81 ± 0.03 $R_\oplus$, $P \simeq 0.789$ days), an inner super-Earth, and WASP-47d (13.1 ± 1.5 $M_\oplus$, 3.58 ± 0.05 $R_\oplus$, $P \simeq 9.031$ days), an outer Neptunian. Around the same time, the results from the first extensive RV campaign (Neveu-VanMalle et al. 2016) revealed the presence of a fourth non-transiting Jupiter-sized planet on a much longer orbit, WASP-47c (1.25 ± 0.03 M_{jup}, $P \simeq 588$ days). Subsequent RV analysis with fresh data have further refined and/or constrained the planetary masses (Dai et al. 2015; Sinukoff et al. 2017; Vanderburg et al. 2017). The opportunity of combining TTV and RV analysis in a joint approach was exploited by Almenara et al. (2016) and Weiss et al. (2017), the former within a photodynamical framework[4]. All the published measurements of planetary masses for WASP-47 are summarized in Table 1. It is worth mentioning that the measurement of the spin-orbit angle obtained through the Rossiter–McLaughlin effect is consistent

with an aligned configuration ($\lambda = 0° \pm 24°$) for WASP-47b (Sanchis-Ojeda et al. 2015) and that a phase-curve re-analysis of K2 photometry constrained the WASP-47b albedo to values significantly lower than the average of HJs (Kane et al. 2020). Lastly, a very recent analysis by Bryant & Bayliss (2022) focusing on the characterization of planet-e has made use of both TESS and ESPRESSO data for the first time.

Despite the extensive amount of work carried out on WASP-47 so far, a convincing and complete description of the evolutionary history of this system is still elusive. Our current understanding of this system will change once the *James Webb* Space Telescope (JWST) enables a detailed atmospheric characterization of WASP-47's transiting planets, especially of the small ones: -e and -d (Bryant & Bayliss 2022). Unfortunately, a reasonably accurate prediction of the future transits of planet-d is difficult, as even the best available ephemerides based on a combination of K2 and RV data will have drifted by about 1 h (1-σ) at epoch 2023.0. The photometric detection of WASP-47d is indeed beyond the reach of ground-based facilities, and TESS has been unable to significantly detect the only transit predicted to fall in Sector 42 (and will not re-observe it at least until the end of Cycle 6 in 2024). The need to recover a new set of reliable ephemerides is one of the initial motivations of our investigation. In addition, the mass measurements of planets -d and -e have historically been slightly inconsistent with each other due to a small statistical tension between the most precise estimate through a photodynamical approach and studies wholly based on RV data (Table 1). Although the most recent ESPRESSO measurements (Bryant & Bayliss 2022) appear to have solved this tension for planet-d (but still not for -e), WASP-47 remains one of the very few systems for which a precise mass measurement can be achieved by either TTVs or RVs, potentially shedding some light on an old debate about a possible systematic discrepancy between the two techniques (Mills & Mazeh 2017; Petigura et al. 2018).

In this paper, we present new data from the CHaracterising ExOPlanet Satellite (CHEOPS) and new ground-based photometric data for WASP-47b and WASP-47d, and we perform a global dynamical re-analysis of all the available data, including the latest TESS and ESPRESSO data sets. We focus particularly on the determination of the orbital and physical parameters of planets -d and -e in order to address the aforementioned issues. In Sect. 2, we describe all the photometric and spectroscopic data

---

2   Source: NASA Exoplanet Archive. https://exoplanetarchive.ipac.caltech.edu/
3   All the M_p, R_p, and P values quoted in this paragraph are consistently borrowed from the analysis by Vanderburg et al. (2017).
4   We refer the reader to Almenara et al. (2015) for a complete description and discussion on the photodynamical approach.

analyzed in this work. In Sect. 3, we deal with the light curve fitting and the dynamical modeling. Finally, we present and discuss our results, including a comparison with the literature, in Sect. 4.

2. Observations

For our dynamical analysis, we gathered all the publicly available RV and photometric data of WASP-47. This included both public data (from K2, TESS, and several RV surveys) and new proprietary data from CHEOPS and ground-based telescopes, described below. A log summarizing all the analyzed photometric data is reported in the Appendix. The time stamps associated with all the measurements were consistently converted to the BJD_{TDB} standard, as prescribed by Eastman et al. (2010).

2.1. CHEOPS photometry

Launched in 2019, CHEOPS (Benz et al. 2021) is an ESA S-class mission currently carrying out its 3.5-yr nominal observing program. The scientific instrument of CHEOPS is a 32-cm reflecting telescope designed to deliver defocused images for the performance of ultra-high-precision photometric measurements of bright stars. The high-performance capabilities of CHEOPS when working with transit timing in particular have been demonstrated by Borsato et al. (2021).

Eleven visits of WASP-47 were scheduled with CHEOPS in 2020 and 2021 within the Guaranteed Time Observations (GTO) programs CH_PR100017 and CH_PR100025 (see Table A.4 for a list of the CHEOPS data sets). Ten visits were centered on the transits of WASP-47b (Table A.1), and one was centered on WASP-47d (Table A.3). All the light curves were extracted from the raw satellite data by the official CHEOPS Data Reduction Pipeline v13.1 (DRP; Hoyer et al. 2020), and their plots are shown in the left panel of Fig. 1 (planet-b) and in Fig. 3 (planet-d). The exposure time was set to 60 s and the minimum efficiency to 50%, resulting in some of the light curves showing noticeable gaps every 98.77 min (the orbital period of CHEOPS) due to the spacecraft crossings of the South Atlantic Anomaly as well as Earth-related constraints (blockage of the line-of-sight by the Earth and high levels of stray light).

2.2. K2 and TESS photometry

During its Campaign 3, K2 monitored WASP-47 in short-cadence mode (net cadence: 58.3 s) for 69 nearly uninterrupted days, from November 14, 2014, to January 23, 2015. These data sets were used to study the transits of planets -d and -e for the first time (Becker et al. 2015). We also use their light curves in our analysis, as they are already corrected for jitter-induced systematic errors by fitting splines as a function of spatial drift, following the procedure by Vanderburg & Johnson (2014). Overall, 108 transit light curves from K2 were ingested in our analysis: 16 of planet -b, seven of planet-d, and 85 of planet-e. These are summarized in Tables A.1, A.3, A.5, and A.6, respectively.

Almost 7 yr later, WASP-47 was observed by TESS for the first time (and the only time so far) in Sector 42 (camera 1, CCD 4), from August 20 to September 16, 2021. Being a known planet host, it was designated as a 120-s cadence target. The resulting data set is the same investigated by Bryant & Bayliss (2022), who used of the Pre-search Data Conditioned Simple Aperture Photometry (PDCSAP) light curve made available by the Science Processing Operations Center (SPOC) pipeline

(Jenkins et al. 2016). Unfortunately, the PDCSAP light curve is missing a large one-week section, including two transits of WASP-47b (on August 27 and 31), due to a "scattered light" quality flag. Unlike Bryant & Bayliss (2022), we based our analysis on Simple Aperture Photometry (SAP) data, where the two missing transits are preserved and do not appear to be impacted by a significant amount of systematic noise, as is demonstrated in Sect. 3.1. While the SAP algorithm does not correct the light curves for photometric dilution due to contaminating sources, we emphasize that no *Gaia* DR3 source (limiting magnitude $G \simeq 21$) is present at all within a radius of 30″ from WASP-47, and the brightest one within 60″ has $G = 17.50$, implying a negligible dilution factor. We also note that a constant dilution factor does not have any systematic effect on the measurement of transit times because it does not alter the symmetry of the transit signal.

Overall, six TESS light curves of planet-b (Table A.1; right panel of Fig. 1) were ingested. As already noted by Bryant & Bayliss (2022), individual transits from planets -d and -e are hidden in the TESS photometric scatter, and their detection is at most marginal. Our preliminary fitting tests confirmed this, and we did not attempt to retrieve their timings. The next visit to WASP-47 by TESS is not expected until at least the end of Cycle 6 (October 2024).

2.3. Ground-based photometry

One transit of WASP-47b was observed on September 24, 2021, by the 60-cm Rapid-Eye Mount telescope (REM; Zerbi et al. 2001) through the ROS2 instrument (Molinari et al. 2014), a charge-coupled device (CCD) camera able to observe the same field of view ($9.1' \times 9.1'$) simultaneously in four photometric bands (Sloan g', r', i', and z'). These observations (PI: Nascimbeni) were carried out as part of the TASTE program, a ground-based multi-site long-term TTV campaign to monitor transiting planets (Nascimbeni et al. 2011). Two bright reference stars (TYC 5805-338-1 and TYC 5805-739-1) were always imaged along with the target, allowing us to perform differential photometry. In addition, in order to mitigate systematic errors from guiding drifts, pixel-to-pixel non-homogeneity, and flat-field errors, a generous amount of defocus was applied ($FWHM \gtrsim 10$ pix).

The four transit light curves from the observation were extracted by running STARSKY (Nascimbeni et al. 2013), the photometric pipeline developed for TASTE. The STARSKY pipeline automatically selects the best combination of photometric aperture radii and weighting scheme to minimize the final out-of-transit scatter. No linear detrending against the external parameters automatically tested by STARSKY proved to be effective (i.e., linear baseline, airmass, x-y position, background level, stellar FWHM). Guiding drifts unfortunately turned out to be much larger than anticipated, totaling more than 30 pixels throughout the whole series. The resulting systematic errors impacted the g', i', and z' data to an unacceptable extent, while the r' light curve was mostly spared, thanks to its much better flat-field correction and its structure being more homogeneous at small spatial scales. For this reason, we only considered the r' light curve (right panel of Fig. 2) for our subsequent analysis.

Seven additional transit light curves of WASP-47b (of six distinct transit events) were collected from 2020 to 2021 by Y. Jongen and A. Wünsche and are available on the public archive of the Exoplanet Transit Database (ETD; Poddaný et al. 2010). They were gathered through an *R* filter with a PlaneWave
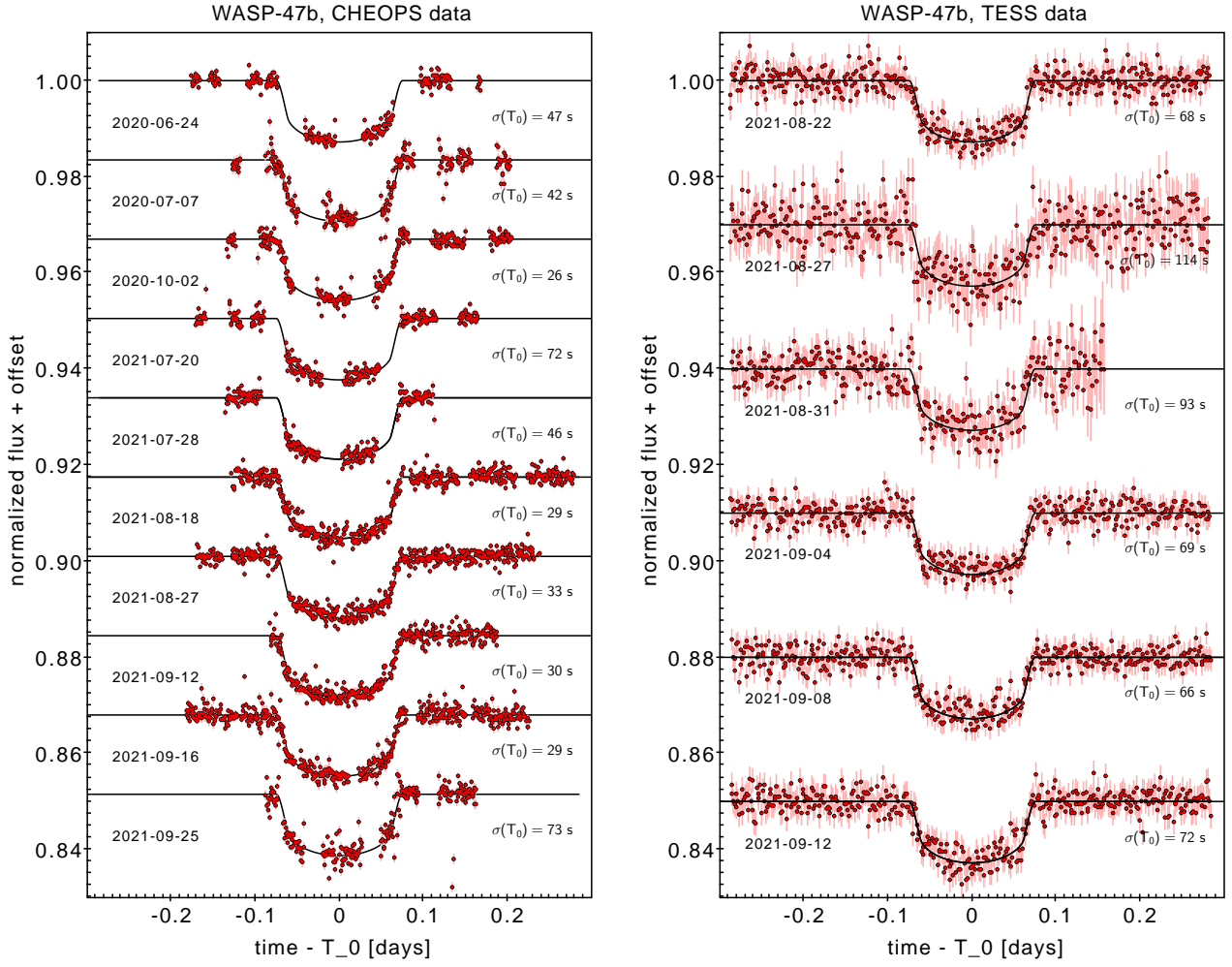
Fig. 1. Space-based light curves of WASP-47b from CHEOPS and TESS analyzed for the present work after de-trending. For each light curve, the corresponding label shows the acquisition date in UT and the timing error σ_{T_0} (in seconds). Arbitrary vertical offsets of 0.0165 and 0.03 were added, respectively, to both sets for visualization purposes.
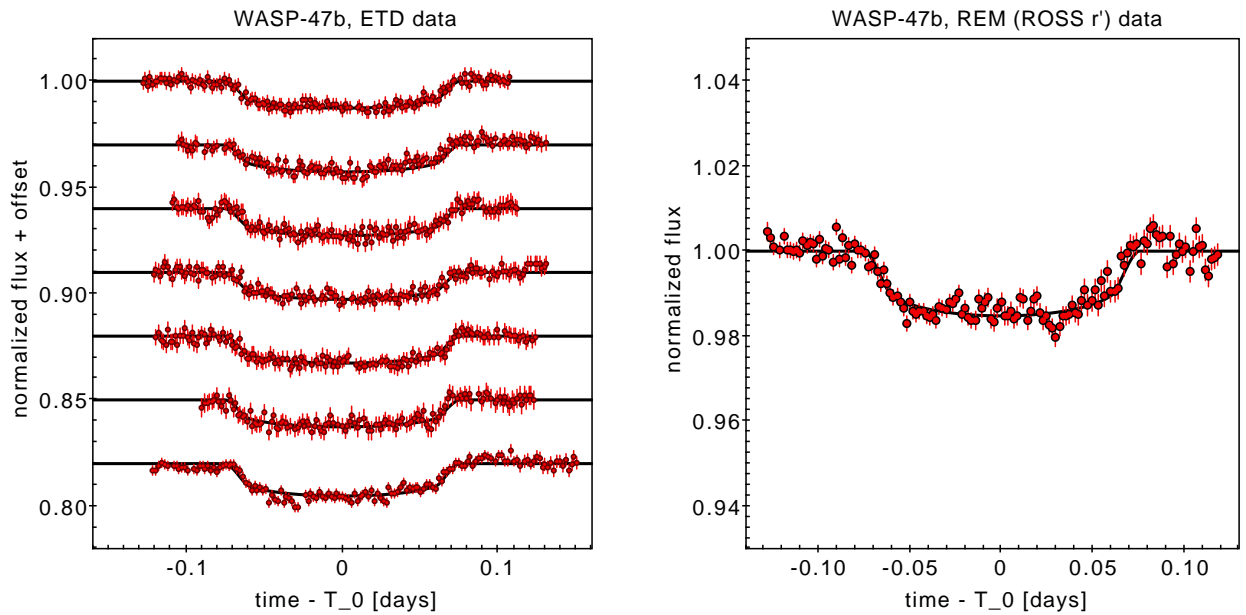

Fig. 2. Ground-based light curves of WASP-47b from ETD and REM analyzed for the present work. An arbitrary vertical offset of 0.03 was added to the ETD light curves for visualization purposes. The light curves are sorted in chronological order (see Table A.2) increasing towards bottom.
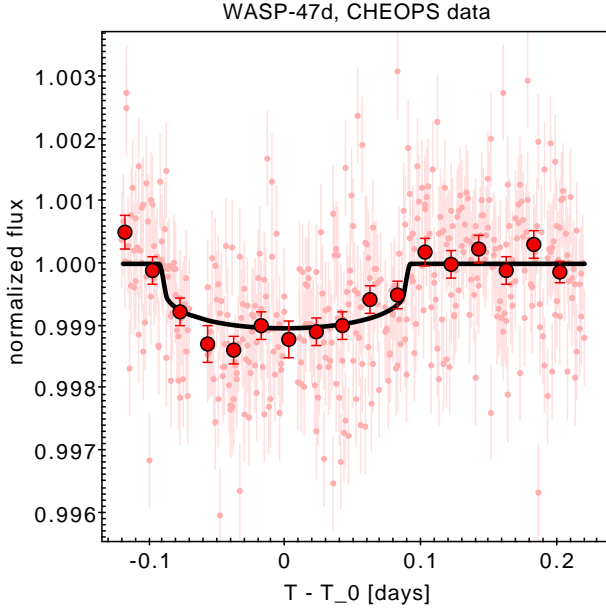
Fig. 3. CHEOPS light curve of WASP-47d after de-trending. The pink data points are at the original sampling cadence (60 s), and the red circles were averaged over 20-min intervals.

CDK 17″ telescope coupled with a Moravian G4 16k CCD camera at the Deep Sky Chile facility (Jongen) and with an unfiltered PlaneWave CDK 20″ telescope coupled with the same camera at the El Sauce Observatory in Chile (Wünsche). The exposure time was set to 120 s by both observers. After visually checking their quality and converting the time stamps to BJD$_{TDB}$, the transit light curves were included in our analysis as well. These light curves are detailed in Table A.2 and plotted in the left panel of Fig. 2.

2.4. Radial velocities

We collected all the available high-precision RV data for our analysis from the scientific literature:
 – 19 from ESPRESSO (Bryant & Bayliss 2022),
 – 47 from HIRES (Sinukoff et al. 2017),
 – 69 from HARPS-N (Vanderburg et al. 2017),
 – 26 from PFS (Dai et al. 2015),
 – 51 from CORALIE (Hellier et al. 2012; Neveu-VanMalle et al. 2016),
for a total of 212 independent data points spanning 9 yr (2010–2019).

3. Data analysis

3.1. Light curve fitting

All the photometric data described in the previous section were homogeneously (re-)analyzed through the PyORBIT (Malavolta et al. 2016, 2018) code. The CHEOPS light curves also went through an additional detrending stage using cheope[5], an optimized python tool (of which pycheops is the back-end; Maxted et al. 2022) specifically developed to filter, correct, and fit CHEOPS data. The detrending model of cheope is defined as a linear combination of terms, including a quadratic baseline $f_0 + df/dt + d^2f/dt^2$, the first and second order derivative

---

Table 2. Stellar and limb darkening parameters adopted in the transit fitting process (Sect. 3.1) and subsequent dynamical analysis (Sect. 3.2).

Stellar parameters		
Mass ($M_\odot$)		1.058 ± 0.047
Radius ($R_\odot$)		1.156 ± 0.009
Limb darkening parameters		
Instrument	u_1	u_2
CHEOPS	0.571 ± 0.020	0.096 ± 0.044
REM (r)	0.558 ± 0.023	0.112 ± 0.054
TESS	0.444 ± 0.016	0.120 ± 0.038
K2	0.562 ± 0.020	0.102 ± 0.044
ETD	0.558 ± 0.023	0.112 ± 0.054

Notes. Both sets of parameters were derived as described in Sect. 3.1.

of the centroid offset in x and y pixel coordinates (df/dx, d^2f/dx^2, df/dy, d^2f/dy^2), background (df/db), contamination ($df/dcontam$), and the first three harmonics of the spacecraft roll angle (in $\cos\phi$ and $\sin\phi$). There is also an additional term called "glint" that empirically models the internal reflections as a spline-based smooth function (Borsato et al. 2021). The combination of terms to be adopted as the best detrending model was selected automatically by cheope according to its Bayes factor, first through an lmfit optimization (Newville et al. 2014) to find a reasonable starting point and then with an emcee fit (Foreman-Mackey et al. 2013).

For both CHEOPS and all the other data sets, the stellar activity signal and any residual instrumental trend were subtracted using wōtan (Hippke et al. 2019) after masking the transits of planets -b, -d, and -e to get the normalized light curves. The filter adopted was a Tukey's bi-weight with a window filter duration set equal to the transit duration plus its 1-σ uncertainty. All the detrended transits from ground- and space-based telescopes are shown in Figs. 1–3. As for the TESS Sector 42 light curves, we focused our analysis on the extraction of six transits of planet -b only, after masking the transits of planets -d and -e, which were only marginally detectable in this data set and hence not usable for an individual T_0 fit.

In order to extract the central transit times T_0, we applied PyORBIT independently on each of the five data sets (i.e., CHEOPS, TESS, K2, REM, and ETD), performing a modeling of each light curve using PyDE+emcee (Parviainen et al. 2016; Foreman-Mackey et al. 2013). We assumed Keplerian orbits for all three fitted planets, -b, -e, and -d. We fixed the $a/R_\star$ parameter of each planet at the values found on the highest S/N data set (K2; Vanderburg et al. 2017), leaving the individual T_0 values, the planetary radius $R_p/R_\star$, and the orbital inclination i for each planet as the only free parameters in order to take into account changes in the impact parameter as a function of time or different transit depths through different instruments and filters. The stellar parameters were derived by the CHEOPS Stellar Characterization team following the procedure described by Borsato et al. (2022), Sect. 3.2.1. The two parameters that are crucial for our dynamical analysis, the stellar radius ($R_\odot$) and mass ($M_\odot$), are listed in Table 2. We adopted a quadratic law u_1, u_2 for the limb darkening coefficients, but we re-parameterized them as fitting parameters q_1 and q_2, as done by Kipping (2013). The priors set on the coefficients u_1 and u_2 are reported in Table 2. We assumed a Gaussian prior distribution over the coefficients

Table 3. Best-fit values of planetary radius R_p (derived from $R_p/R_\star$) and orbital inclination i.

Parameter	WASP-47b	WASP-47d	WASP-47e
CHEOPS			
R_p ($R_\oplus$)	12.72 ± 0.12	3.88 ± 0.20	–
i (°)	89.21 ± 0.51	89.23 ± 0.51	–
TESS			
R_p ($R_\oplus$)	12.61 ± 0.17	–	–
i (°)	88.6 ± 0.6	–	–
K2			
R_p ($R_\oplus$)	12.86 ± 0.10	3.65 ± 0.03	1.83 ± 0.02
i (°)	89.00 ± 0.17	89.23 ± 0.10	86.73 ± 1.76
ETD			
R_p ($R_\oplus$)	12.95 ± 0.17	–	–
i (°)	89.06 ± 0.58	–	–
REM			
R_p ($R_\oplus$)	13.64 ± 0.28	–	–
i (°)	87.86 ± 0.45	–	–

Notes. All these parameters were fitted as common parameters among individual data sets. See Sect. 3.1 for details about the transit fit.

for all the instruments using a bi-linear interpolation of the limb-darkening profile defined in Claret (2017, 2021).

We used PyDE to find the best starting point for the MCMC sampler. For each data set, PyDE used a population size of $4 \times N_{par}$, where N_{par} is the number of free parameters, and let it evolve for 64 000 generations, and for the Bayesian sampler, we set 100 chains for 150 000 steps, discarding the first 40 000 by adopting a thinning factor of 100. All the final T_0 values of this analysis are summarized in Tables A.1 to A.6, while the physical best-fit values of the common parameters among individual data sets (R_p, i) are shown in Table 3. As anticipated in Sect. 2, we directly compared the transit timings we extracted from TESS SAP photometry with those obtained from the PDCSAP light curves by Bryant & Bayliss (2022) and listed in their Table 4 to check for any systematic offset. The average $\Delta T_0 = T_{0,\mathrm{PDCSAP}} - T_{0,\mathrm{SAP}}$ evaluated over the four transits in common yielded 14 s (with average error bars of ~66 s), and no pair disagreed by more than $0.5\,\sigma$. In other words, timings from SAP and PDCSAP are in perfect statistical agreement.

3.2. Dynamical modeling

We employed the TRADES dynamical integrator (Borsato et al. 2014), which has already been successfully applied to Kepler/K2 (Borsato et al. 2019) and CHEOPS data (Borsato et al. 2021) as well as to simulate the Ariel TTV science case (Borsato et al. 2022). The TRADES dynamical integrator allowed us to fit transit times (T_0) and RVs simultaneously during the integration of the orbits. We fitted the mass ratios ($M_p/M_\star$), the periods (P), and the mean longitude (λ) for all the planets. The eccentricity (e) and the argument of periastron (ω) were fitted as ($\sqrt{e}\cos\omega$, $\sqrt{e}\sin\omega$) for planets -b, -c, and -d, while we used the (initial) circular orbit ($e = 0$, $\omega = 90°$) for planet-e due to its extremely short tidal circularization timescale (Vanderburg et al. 2017). We adopted our initial values for M_b, M_c, M_d, M_e, e and ω from Almenara et al. (2016). We fixed the longitude of

the ascending node (Ω) of -b, -c, and -e to 180°. For the orbital inclination i, we took the weighted average of the fitted values from Sect. 3.1 and Table 3 (for instance, $i_b = 88.88 \pm 0.14°$). We found that by assuming $i_d < 90°$, one of the most recent transits of planet-b was missed by our integration (i.e., the impact parameter for that transit was greater than one). Almenara et al. (2016) reported a best-fit inclination higher than 90°, but the authors specified that the supplementary angle is equally probable. If both planets -b and -d transit in the same stellar hemisphere (with respect to the observer's line of sight), then their relative distance would be shorter with respect to the case with planet-d on the opposite hemisphere. The mutual gravitational interaction would of course be much stronger in the former case, moving planet-b on some occasions to a non-transiting configuration that is not observed in our data. Therefore, we assumed that planet-d transits the opposite hemisphere with respect to -b ($i_b < 90°$) and adopted the value $180° - i_d$ as the initial parameter for TRADES. We also fitted the i and Ω of -d, and we set i_c to 90°. All the orbital parameters are astrocentric and defined at the reference time 2456979.5 BJD_TDB, the same as in Almenara et al. (2016). The initial periods were set to the linear ephemeris fitted to T_0s determined in Sect. 3.1. For each RV data set, we fitted a $\log_2$-based jitter and an RV offset (γ). However, we found that changing the starting point of the jitter (e.g., $\log_2$ of 0.5 and $<1 \times 10^{-6}\,\mathrm{m\,s^{-1}}$) did not affect the final distribution of the chains and, therefore, did not change the best-fit solution. We split the CORALIE data set into three subsets, as done in Almenara et al. (2016), for a total of seven RV data sets. In all, we fitted 34 parameters, all with uniform-uninformative priors in the parameter space.

In order to save computational time, we first ran a local minimizer[6] and used the result as a starting point for the python package emcee (Foreman-Mackey et al. 2013, 2019), for which we initialized 68 walkers with a tight Gaussian. We adopted as a sampler algorithm a mix of the differential evolution proposal (80% of the walkers; Nelson et al. 2014) and the snooker differential evolution proposal (20% of the walkers; ter Braak & Vrugt 2008). We let the code run for 110 000 steps and discarded the first 100 000 steps as burn-in after checking the convergence of the chains by means of visual inspection as well as through diagnostics from Geweke (1991, within 2-3σ) and Gelman-Rubin statistics[7] (Gelman & Rubin 1992). Our uncertainties are computed as the high density interval (HDI) at 68.27% from the posterior distribution as the equivalent of the credible intervals at the 16th and 84th percentile. We defined our best-fit solution as the maximum likelihood estimator (MLE), that is, the parameter sample that maximizes the log-likelihood ($\log \mathcal{L}$) of the posterior distribution within the HDI. We also computed a symmetric uncertainty (σ) as the 68.27th percentile of the (sorted) absolute residuals of the posterior with respect to the best-fit solution (see Table 4 for a summary of the fitted and physical parameters of the system determined with TRADES. See the O–C diagrams of planets -b, -d, and -e in Figs. 4–6 and the RV plot in Fig. 7.)

4. Discussion and conclusions

The global analysis presented in this work is the most comprehensive dynamical modeling of the WASP-47 planetary system

---

[6] Nelder-Mead method implemented in the scipy.optimize.minimize function.

[7] The $\hat{R}$ statistic reached 1.01, but we note that this statistic is not effective with the sampling algorithm we used.

Table 4. Summary of the best-fit MLE parameters for the WASP-47 system determined with TRADES.

Parameter (unit)	MLE (HDI & σ)	Priors
planet b		
$M_{\rm p}/M_\star$ ($M_\odot/M_\star \times 10^{-3}$)	$1.0617^{+0.0015}_{-0.0007} \pm 0.0012$	
P (days)	$4.158548^{+0.000008}_{-0.000017} \pm 0.000013$	$\mathcal{U}(3.8, 4.5)$
$\sqrt{e}\cos\omega$	$0.0005^{+0.0042}_{-0.0091} \pm 0.007$	
$\sqrt{e}\sin\omega$	$0.0239^{+0.009}_{-0.004} \pm 0.007$	
λ (°)	$329.05^{+0.03}_{-0.01} \pm 0.02$	$\mathcal{U}(0, 360)$
$M_{\rm p}$ ($M_\oplus$)	$374^{+17}_{-16} \pm 17$	$\mathcal{U}(80, 636)$
e	$0.0006^{+0.0005}_{-0.0002} \pm 0.0004$	$\mathcal{U}(0.0, 0.5)$
ω (°)	$89^{+19}_{-11} \pm 17$	$\mathcal{U}(0, 360)$
$\mathcal{M}$ (°)	$60^{+11}_{-19} \pm 17$	$\mathcal{U}(0, 360)$
planet c		
$M_{\rm p}/M_\star$ ($M_\odot/M_\star \times 10^{-3}$)	$1.270^{+0.005}_{-0.017} \pm 0.012$	
P (days)	$589.57^{+0.02}_{-0.02} \pm 0.02$	$\mathcal{U}(560, 600)$
$\sqrt{e}\cos\omega$	$-0.19060^{+0.00001}_{-0.02} \pm 0.015$	
$\sqrt{e}\sin\omega$	$0.478^{+0.007}_{-0.016} \pm 0.014$	
λ (°)	$166.02^{+0.03}_{-0.01} \pm 0.02$	$\mathcal{U}(0, 360)$
$M_{\rm p}$ ($M_\oplus$)	$447^{+18}_{-22} \pm 20$	$\mathcal{U}(159, 636)$
e	$0.264^{+0.007}_{-0.012} \pm 0.011$	$\mathcal{U}(0.0, 0.5)$
ω (°)	$111.8^{+2.7}_{-0.2} \pm 2$	$\mathcal{U}(0, 360)$
$\mathcal{M}$ (°)	$234.3^{+0.2}_{-2.7} \pm 2$	$\mathcal{U}(0, 360)$
planet d		
$M_{\rm p}/M_\star$ ($M_\odot/M_\star \times 10^{-3}$)	$0.0440^{+0.0007}_{-0.0017} \pm 0.0013$	
P (days)	$9.09577^{+0.00016}_{-0.00008} \pm 0.00013$	$\mathcal{U}(8.7, 9.3)$
$\sqrt{e}\cos\omega$	$0.0037^{+0.0017}_{-0.0115} \pm 0.009$	
$\sqrt{e}\sin\omega$	$0.031^{+0.016}_{-0.006} \pm 0.012$	
λ (°)	$278.61^{+0.04}_{-0.01} \pm 0.03$	$\mathcal{U}(0, 360)$
i (°)	$90.805^{+0.020}_{-0.014} \pm 0.018$	$\mathcal{U}(80, 100)$
Ω (°)	$179.954^{+0.006}_{-0.012} \pm 0.010$	$\mathcal{U}(0, 360)$
$M_{\rm p}$ ($M_\oplus$)	$15.5^{+0.7}_{-0.9} \pm 0.8$	$\mathcal{U}(1, 159)$
e	$0.0010^{+0.0008}_{-0.0007} \pm 0.0008$	$\mathcal{U}(0.0, 0.5)$
ω (°)	$83^{+18}_{-3} \pm 14$	$\mathcal{U}(0, 360)$
$\mathcal{M}$ (°)	$16^{+10}_{-15} \pm 14$	$\mathcal{U}(0, 360)$
planet e		
$M_{\rm p}/M_\star$ ($M_\odot/M_\star \times 10^{-3}$)	$0.0254^{+0.0010}_{-0.0003} \pm 0.0008$	
P (days)	$0.789608^{+0.000002}_{-0.000001} \pm 0.000001$	$\mathcal{U}(0.7, 0.86)$
λ (°)	$149.074^{+0.015}_{-0.033} \pm 0.03$	$\mathcal{U}(0, 360)$
$M_{\rm p}$ ($M_\oplus$)	$9.0^{+0.6}_{-0.4} \pm 0.5$	$\mathcal{U}(1, 80)$
$\mathcal{M}$ (°)	$244.15^{+0.015}_{-0.033} \pm 0.025$	$\mathcal{U}(0, 360)$
RV data-sets		
$\gamma_{\rm CORALIE1}$ (m s^{-1})	$-27069^{+3}_{-2} \pm 2$	
$\gamma_{\rm CORALIE2}$ (m s^{-1})	$-27084.9^{+0.4}_{-4.2} \pm 3.2$	
$\gamma_{\rm CORALIE3}$ (m s^{-1})	$-27065^{+8}_{-2} \pm 6$	
$\gamma_{\rm PFS}$ (m s^{-1})	$17.80^{+1.20}_{-0.09} \pm 0.8$	
$\gamma_{\rm HIRES}$ (m s^{-1})	$4.6^{+0.2}_{-0.6} \pm 0.5$	
$\gamma_{\rm HARPS}$ (m s^{-1})	$-27041.1^{+0.4}_{-0.3} \pm 0.3$	
$\gamma_{\rm ESPRESSO}$ (m s^{-1})	$-27165.7^{+0.1}_{-0.5} \pm 0.3$	

Notes. The columns give the name of the parameter, its best-fit value with its associated 68.27% HDI and σ, and the priors adopted. Astrocentric orbital parameters are defined at 2456979.5 BJD$_{\rm TDB}$. $\mathcal{M}$ is the mean anomaly computed as $\mathcal{M} = \lambda - \omega - \Omega$. We fixed the value of $i_{\rm c} = 90°$, so $M_{\rm p}$ of planet -c is the minimum mass. Planet -e has a circular orbit ($e = 0$, $\omega = 90°$) at the reference time, so e and ω have not been fitted with TRADES. See Sect. 3.2 for details.
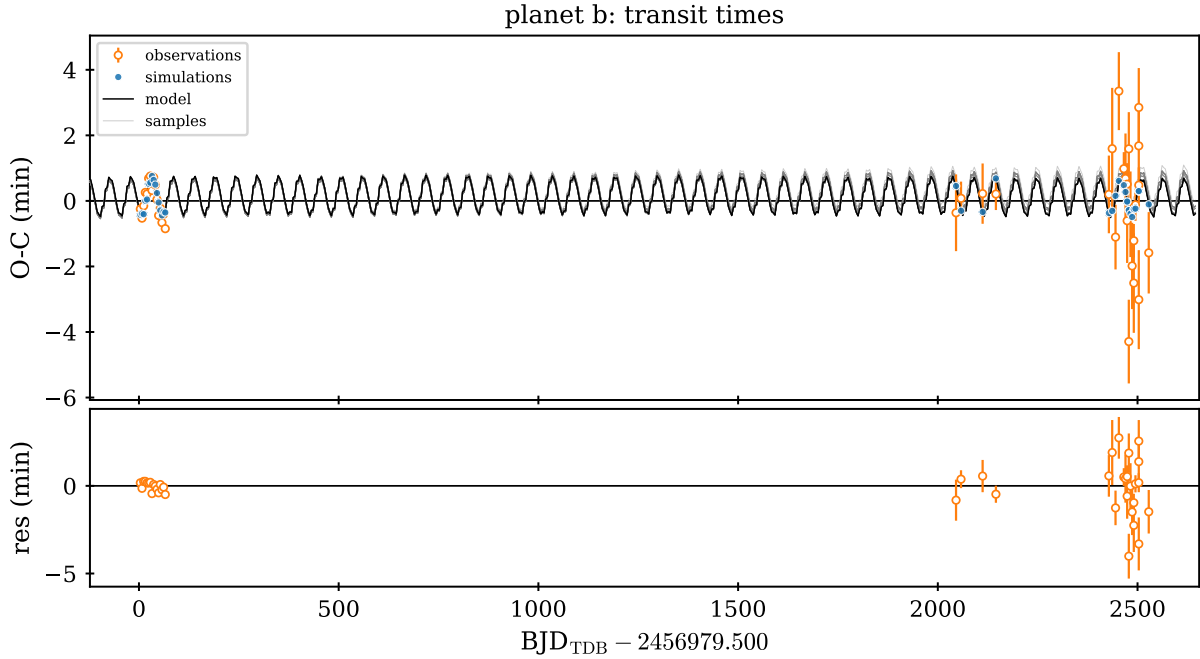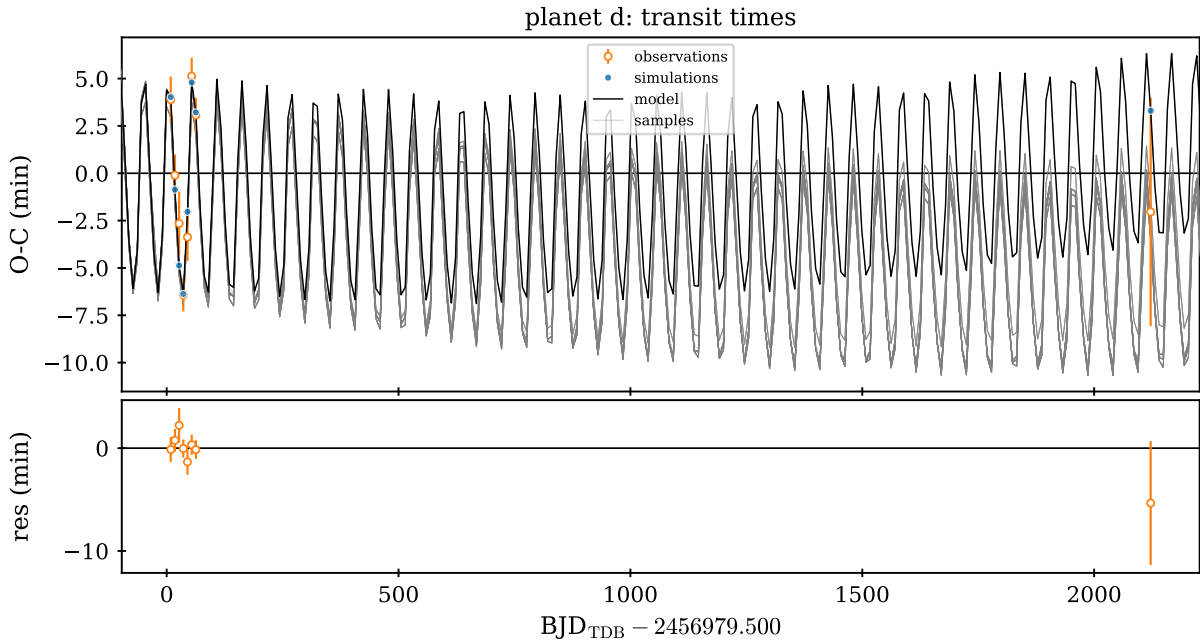
planet b: transit times

Fig. 4. Transit times of WASP-47b. Upper panel: observed – calculated (O–C) diagram. The O–C was calculated by subtracting the predicted T_0 calculated from the linear ephemeris to the observed transit times. The O–C values computed from the observed T_0s are plotted as open orange circles, while the O–C of the TRADES-simulated T_0s from the best-fit model are plotted as blue circles. Samples drawn from the posterior distribution within HDI are shown as grey lines. Lower panel: residuals computed as the difference between observed and simulated T_0s.

planet d: transit times

Fig. 5. Transit times of WASP-47d. Upper panel: observed – calculated (O–C) diagram. The O–C was calculated by subtracting the predicted T_0 calculated from the linear ephemeris to the observed transit times. The O–C values computed from the observed T_0s are plotted as open orange circles, while the O–C of the TRADES-simulated T_0s from the best-fit model are plotted as blue circles. Samples drawn from the posterior distribution within HDI are shown as grey lines. Lower panel: Residuals computed as the difference between observed and simulated T_0s.

carried out so far. We exploited all the available RV and TTV data sets and merged them with 19 unpublished light curves, 11 of which were observed with CHEOPS. Our newly derived planetary masses (M_b, M_c, M_d, and M_e) from the final best-fit parameters (Table 4) can be compared with the values reported in the literature and listed in Table 1.

For the two low-mass planets (-d, -e), we found best-fit masses ($M_d/M_\oplus = 15.5 \pm 0.8$, $M_e/M_\oplus = 9.0 \pm 0.5$) with relative errors of about 5%, which is smaller than all the previous

relative errors and is now limited mostly by our knowledge of the stellar mass (relative error on $M_\star$: ~4%). In particular, for the innermost planet, our solution is perfectly consistent with the upper extreme $M_e/M_\oplus = 9.1 \pm 1.0$ set by Weiss et al. (2017, joint RV plus TTV analysis), but it is not consistent with the lower extreme $M_e/M_\oplus = 6.8 \pm 0.6$ set by Bryant & Bayliss (2022) using RVs only, apparently confirming, at 2.8σ significance, some kind of systematic offset between the two techniques (Mills & Mazeh 2017; Petigura et al. 2018). We did not see a similar
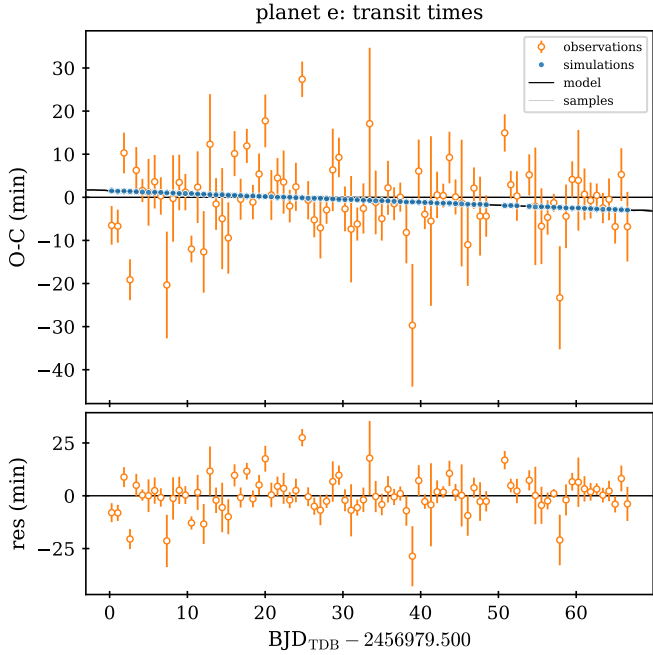
Fig. 6. Transit times of WASP-47e. Elements are the same as in Figs. 4 and 5, but for planet -e.

behavior for planet -d, whose best-fit mass is fully consistent with all the previous measurements but more precise. By calculating the bulk densities as derived quantities from Table 4 and propagating the errors, we get $\rho_d = 1.69 \pm 0.22\,\mathrm{g\,cm^{-3}}$ and $\rho_e = 8.1 \pm 0.5\,\mathrm{g\,cm^{-3}}$, thus confirming a Neptune-like density and composition for planet -d (implying an extended volatile envelope) but also moving planet -e very close to what planetary structure models predict to be an Earth-like composition rather than a pure-silicate one (in contrast to the claims by Vanderburg et al. 2017 and Bryant & Bayliss 2022; see Fig. 8). If that conclusion were true, then planet -e would not appear as an outlier in the planetary density versus stellar irradiation diagram anymore and there would be no reason to hypothesize a different formation path with respect to other ultra-short period planets at similar irradiation levels, such as K2-141b and HD 213885b (Malavolta et al. 2018; Espinoza et al. 2020). Moreover, WASP-47 is a rather metal-rich star at [Fe/H] = +0.36 ± 0.05, according to Mortier et al. (2013). The high density of WASP-47e, which fits into the "super-Mercury" class, would confirm the finding by Adibekyan et al. (2021) that the bulk density of super-Earths correlates with stellar iron fraction. On the other hand, the relatively low density of planet -d would also confirm the trend discovered by Wilson et al. (2022), who found that sub-Neptunes around metal-rich stars have, on average, lower densities. Taken together, our findings would support the general idea that a higher stellar metallicity leads to forming planets with larger cores and, hence, generates denser hot super-Earths (such as -e) and warm sub-Neptunes that are able to retain more extended atmospheric envelopes (-d).

We caution, however, that the existing tension on M_e could be due to subtle methodological biases in RV and/or RV plus TTV analyses that are yet to be fully explored and a deeper understanding of the effects at play in such dynamically complex systems is needed. This is true of course for not only WASP-47 but for all planetary systems for which both techniques can be applied and that are steadily growing in number, especially after the launch of K2 and TESS. Two factors are most frequently discussed when dealing with such issues: the impact of stellar

activity and the way RV and TTV information is merged at the analysis stage. Notably, WASP-47 is not a particularly active star, and all the studies up to and including Vanderburg et al. (2017) explicitly neglected any contribution from stellar activity on both photometric and spectroscopic data. Bryant & Bayliss (2022), on the other hand, noticed an excess scatter in the ESPRESSO data and concluded that the inclusion of a Gaussian process kernel in their RV modeling was justified by a lower BIC value of their fit, even though the statistical significance of the peak on the periodogram of the RV residuals at the claimed rotational period is marginal. The treatment of stellar activity, however, does not appear to be the (only) explanation for the M_e discrepancy we see since Bryant & Bayliss (2022) came to a value that is almost identical to that reported by Vanderburg et al. (2017) without modeling for it: $M_e = 6.8 \pm 0.7$ versus $6.8 \pm 0.6\,M_\oplus$. Beyond that, in an RV plus TTV study such ours, it is extremely difficult to model stellar activity in a consistent framework because the two techniques are effected in different ways and at different timescales (Boisse et al. 2011; Oshagh et al. 2013; Ioannidis et al. 2016); indeed, transit light curves are impacted more by the local rather than global distribution of star spots over the photosphere. With WASP-47, an additional issue prevents us from adopting a more complicated data model (i.e., including stellar activity and/or a photodynamical approach): computational time. Having to deal with four planets, 34 free parameters, and an extensive set of 133 transits and 212 RVs, each of the MCMC steps of the optimization process described in Sect. 3.2 took about 15 s on a medium-power computing workstation, and the whole fit required weeks to reach convergence. This sizable computing time is mostly due to an unfortunate combination of a very long observing baseline (15 yr) and the very short period of the inner planet ($P_e \simeq 0.79$ day), forcing the N-body integration time step to unusually small values. Of course, under these assumptions, the inclusion of a Gaussian process treatment of stellar activity or, even worse, the implementation of a photodynamical algorithm would increase the computational time up to an unreasonable amount, at least with ordinarily available hardware. We emphasize, however, that our result agrees with previous RV plus TTV studies both based (Almenara et al. 2016) and not based (Weiss et al. 2017) on a photodynamical approach, so fitting our light curves and performing the dynamical modeling at separate stages cannot be the sole reason for the discrepancy discussed above.

As for the giant planets (-b and -c), it is worth noting that our newly derived masses are compatible with those presented by Vanderburg et al. (2017) and Bryant & Bayliss (2022) and statistically consistent with all the previous measurements reported in Table 1. The precision of our values $M_b/M_\oplus = 374 \pm 17$, $M_c/M_\oplus = 447 \pm 20$ is larger by a factor of about two with respect to the most recent RV works. This is easily understood if we consider that our error on $M_\star$ (4.4%) is larger than theirs (3%) and our dynamical analysis probes are $M_p/M_\star$ rather than $M_p/M_\star^{2/3}$, the latter being true for a pure RV analysis. In other words, our study is more sensitive to the uncertainty on stellar mass. The same is true for the derived planetary density $\rho_b = 0.98 \pm 0.09\,\mathrm{g\,cm^{-3}}$.

An important byproduct of our analysis is the derivation of new, updated mean ephemerides[8] for all the WASP-47 transiting planets, as this data can be exploited by any future follow-up

---

[8] It is worth noting that the mean ephemeris, by definition, does not account for the TTV modulation. The latter will manifest itself as a (quasi-)periodic term added to the ephemeris with amplitudes $A_{\mathrm{TTV,b}} \simeq 0.7$ min and $A_{\mathrm{TTV,d}} \simeq 5.8$ min.
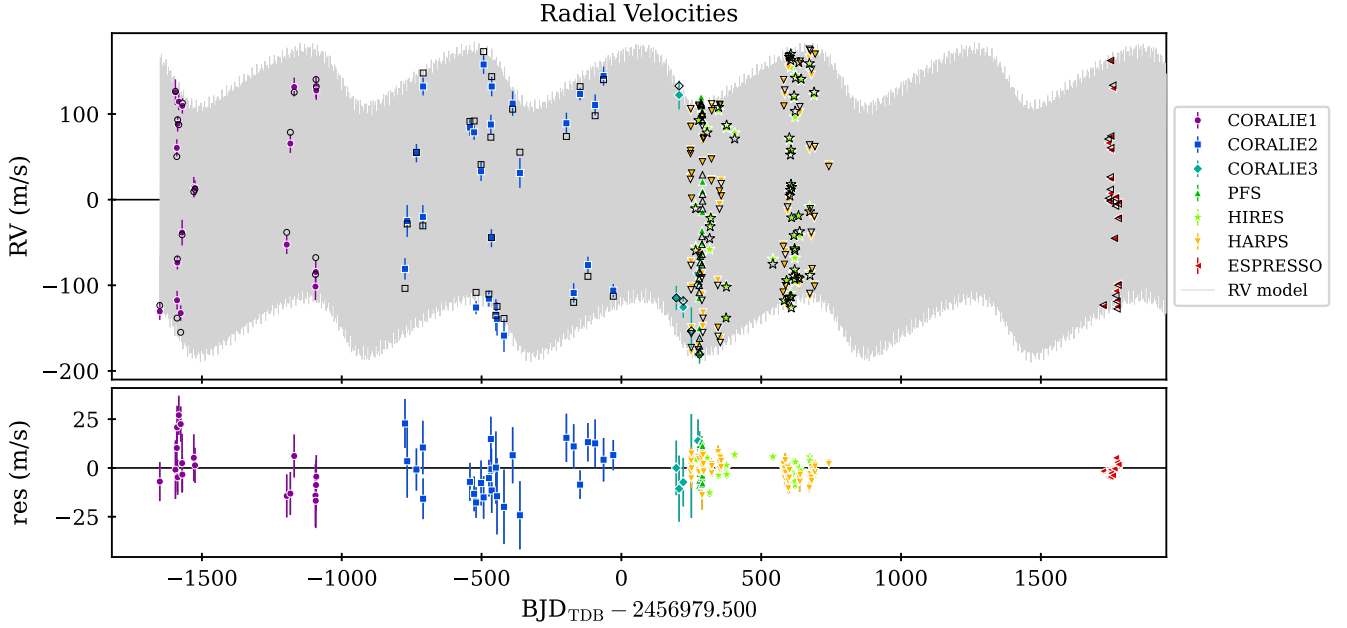
Radial Velocities

Fig. 7. Radial velocities of WASP-47. Upper panel: RV plot. There is a different marker and color for each data set. The TRADES best-fit RV model is plotted with open black shapes. The maximum-likelihood orbital solution is shown by a light gray line. The CORALIE data set was divided into three data sets, as described in Almenara et al. (2016). Lower panel: RV residuals with respect to the TRADES RV best-fit model. The corresponding jitter determined from the best-fit model has been added in quadrature to the measured uncertainty of each data point.

study. Our best-fit relations are:

$$T_{0,b} = 2459407.761987 \pm 0.0000002 \, \text{BJD}_{\text{TDB}} \quad (1)$$
$$+ N \times (4.159151 \pm 0.0000004),$$

$$T_{0,d} = 2457024.430107 \pm 0.0000003 \, \text{BJD}_{\text{TDB}} \quad (2)$$
$$+ N \times (9.030501 \pm 0.000013),$$

$$T_{0,e} = 2457012.13666 \pm 0.00003 \, \text{BJD}_{\text{TDB}} \quad (3)$$
$$+ N \times (0.78961 \pm 0.00003),$$

where N is an integer number commonly known as "epoch" and set arbitrarily to zero at our reference transit time T_{ref}. We highlight that the 1σ uncertainty on transit prediction at 2023.0 for planet -d has now been reduced from about 1 h to just 6 min. Of course this is crucial for planning space-based observations, where the cost of the invested observing time and the time-sensitive nature of the observations makes pinpointing the transit window as precisely as possible critical.

Observations of WASP-47 are not yet scheduled with JWST, at least during Cycle 1, even though its transiting planets -e, -b, and -d have been recognized as suitable targets for transmission spectroscopy (Bryant & Bayliss 2022) and will very likely be proposed in the next cycles. Such observations will be crucial to test our planetary formation theories. It is widely accepted that three main channels for HJ migration exist (Dawson & Johnson 2018): one is through the protoplanetary disk at low eccentricity, another is through high-eccentricity dynamical migration with tidal damping at later times, and the third is through in situ formation close to or at the final orbit. A planet migrating through the disc or having formed in situ would accrete a large amount of gas from inside the ice line, whereas an HJ that migrated dynamically may have originated from beyond the ice line with a different composition (Öberg et al. 2011; Madhusudhan et al.

2017; Knierim et al. 2022). Simulations show that the dynamical migration channel would invariably destroy any close-in planets, as the orbit of the HJ would intersect with that of the close-in planets prior to circularization (Mustill et al. 2015). Thus, unlike ordinary HJs, for very rare systems such as WASP-47, we can rule out one of the main scenarios and test the other models through detailed atmospheric characterization.

Other space-based follow-up opportunities include, at least in principle, TESS, PLATO (Rauer et al. 2014), and ARIEL (Tinetti et al. 2018). As for TESS, we mentioned in the introduction that no other sector will include WASP-47, at least up to the end of Cycle 6, implying that this target will not be re-observed until fall 2024, at best. Unfortunately, individual transits of planets -e and -d are essentially undetectable by TESS due to its noise properties, and the time baseline of each sector is limited to about four weeks. Future sectors, if any, will thus not be effective in significantly extending the TTV analysis carried out so far.

On the other hand, PLATO will be able to deliver high-precision transit light curves of planets -e and -d since the predicted noise level ranges from 90 to 180 ppm in 1 h, according to the number of co-pointing PLATO cameras involved (Montalto et al. 2021). Due to its very low ecliptic latitude, WASP-47 will not lie within the proposed Long-duration Observing Phase fields of PLATO (Nascimbeni et al. 2022), where targets will be continuously observed for at least 2 yr. However, WASP-47 could be selected for the Short-duration Observing Phase and monitored for two to three months without any significant interruption (see Fig. 1 of Heller et al. 2022).

As a closing note, ARIEL, though focused on the atmospheric characterization of exoplanets through emission and transmission spectroscopy (Tinetti et al. 2021), has also been proposed as a very powerful instrument to investigate TTVs (Borsato et al. 2022). WASP-47 is consistently included in the provisional ARIEL target list (Zingales et al. 2018; Edwards & Tinetti 2022) as a "Tier 2" object (aim: in-depth atmospheric characterization through repeated observations), but
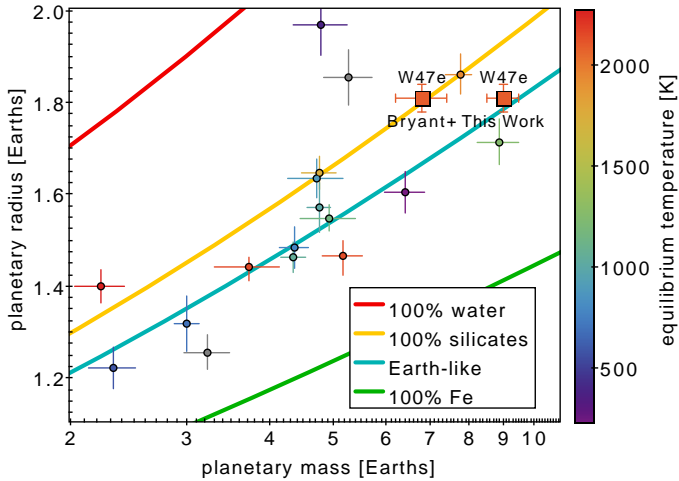
Fig. 8. Mass-radius diagram with all the known planets with a relative error on bulk density better than 20% (circle points) color coded according to their equilibrium temperature. The colored lines represent models at different bulk compositions from Zeng et al. (2019). The two measurements of WASP-47e by us and by Bryant & Bayliss (2022) are plotted as squares.

these observations are only devoted to observing eclipses of planet -b.

References

Adibekyan, V., Dorn, C., Sousa, S. G., et al. 2021, Science, 374, 330
Akeson, R. L., Chen, X., Ciardi, D., et al. 2013, PASP, 125, 989
Almenara, J. M., Díaz, R. F., Mardling, R., et al. 2015, MNRAS, 453, 2644
Almenara, J. M., Díaz, R. F., Bonfils, X., & Udry, S. 2016, A&A, 595, A5
Auvergne, M., Bodin, P., Boisnard, L., et al. 2009, A&A, 506, 411
Becker, J. C., Vanderburg, A., Adams, F. C., Rappaport, S. A., & Schwengeler, H. M. 2015, ApJ, 812, L18
Benz, W., Broeg, C., Fortier, A., et al. 2021, Exp. Astron., 51, 109
Boisse, I., Bouchy, F., Hébrard, G., et al. 2011, A&A, 528, A4
Borsato, L., Marzari, F., Nascimbeni, V., et al. 2014, A&A, 571, A38
Borsato, L., Malavolta, L., Piotto, G., et al. 2019, MNRAS, 484, 3233
Borsato, L., Piotto, G., Gandolfi, D., et al. 2021, MNRAS, 506, 3810
Borsato, L., Nascimbeni, V., Piotto, G., & Szabó, G. 2022, Exp. Astron., 53, 635
Borucki, W. J., Koch, D., Basri, G., et al. 2010, Science, 327, 977
Bryant, E. M., & Bayliss, D. 2022, AJ, 163, 197
Cañas, C. I., Wang, S., Mahadevan, S., et al. 2019, ApJ, 870, L17
Charbonneau, D., Brown, T. M., Latham, D. W., & Mayor, M. 2000, ApJ, 529, L45
Charbonneau, D., Brown, T. M., Noyes, R. W., & Gilliland, R. L. 2002, ApJ, 568, 377
Claret, A. 2017, A&A, 600, A30
Claret, A. 2021, RNAAS, 5, 13
Dai, F., Winn, J. N., Arriagada, P., et al. 2015, ApJ, 813, L9
Dawson, R. I., & Johnson, J. A. 2018, ARA&A, 56, 175
Eastman, J., Siverd, R., & Gaudi, B. S. 2010, PASP, 122, 935
Edwards, B., & Tinetti, G. 2022, AJ, 164, 15

Espinoza, N., Brahm, R., Henning, T., et al. 2020, MNRAS, 491, 2982
Foreman-Mackey, D., Hogg, D. W., Lang, D., & Goodman, J. 2013, PASP, 125, 306
Foreman-Mackey, D., Farr, W., Sinha, M., et al. 2019, J. Open Source Softw., 4, 1864
Fortney, J. J., Dawson, R. I., & Komacek, T. D. 2021, J. Geophys. Res. (Planets), 126, e06629
Gelman, A., & Rubin, D. B. 1992, Stat. Sci., 7, 457
Geweke, J. F. 1991, Evaluating the accuracy of sampling-based approaches to the calculation of posterior moments, Staff Report 148, Federal Reserve Bank of Minneapolis
Hartman, J. D., & Bakos, G. Á. 2016, Astron. Comput., 17, 1
Heller, R., Harre, J.-V., & Samadi, R. 2022, A&A, 665, A11
Hellier, C., Anderson, D. R., Collier Cameron, A., et al. 2012, MNRAS, 426, 739
Henry, G. W., Marcy, G. W., Butler, R. P., & Vogt, S. S. 2000, ApJ, 529, L41
Hippke, M., David, T. J., Mulders, G. D., & Heller, R. 2019, AJ, 158, 143
Hord, B. J., Colón, K. D., Kostov, V., et al. 2021, AJ, 162, 263
Hord, B. J., Colón, K. D., Berger, T. A., et al. 2022, AJ, 164, 13
Hoyer, S., Guterman, P., Demangeon, O., et al. 2020, A&A, 635, A24
Huang, C., Wu, Y., & Triaud, A. H. M. J. 2016, ApJ, 825, 98
Huang, C. X., Quinn, S. N., Vanderburg, A., et al. 2020, ApJ, 892, L7
Ioannidis, P., Huber, K. F., & Schmitt, J. H. M. M. 2016, A&A, 585, A72
Jenkins, J. M., Twicken, J. D., McCauliff, S., et al. 2016, SPIE Conf. Ser., 9913, 99133E
Kane, S. R., Fetherolf, T., & Hill, M. L. 2020, AJ, 159, 176
Kipping, D. M. 2013, MNRAS, 435, 2152
Knierim, H., Shibata, S., & Helled, R. 2022, A&A, 665, A5
Knutson, H. A., Fulton, B. J., Montet, B. T., et al. 2014, ApJ, 785, 126
Latham, D. W., Rowe, J. F., Quinn, S. N., et al. 2011, ApJ, 732, L24
Madhusudhan, N., Bitsch, B., Johansen, A., & Eriksson, L. 2017, MNRAS, 469, 4102
Malavolta, L., Nascimbeni, V., Piotto, G., et al. 2016, A&A, 588, A118
Malavolta, L., Borsato, L., Granata, V., et al. 2017, AJ, 153, 224
Malavolta, L., Mayo, A. W., Louden, T., et al. 2018, AJ, 155, 107
Maxted, P. F. L., Ehrenreich, D., Wilson, T. G., et al. 2022, MNRAS, 514, 77
Mayor, M., & Queloz, D. 1995, Nature, 378, 355
Mills, S. M., & Mazeh, T. 2017, ApJ, 839, L8
Molinari, E., Covino, S., Crimi, G., et al. 2014, SPIE Conf. Ser., 9147, 91476X
Montalto, M., Piotto, G., Marrese, P. M., et al. 2021, A&A, 653, A98
Mortier, A., Santos, N. C., Sousa, S. G., et al. 2013, A&A, 558, A106
Mustill, A. J., Davies, M. B., & Johansen, A. 2015, ApJ, 808, 14
Nascimbeni, V., Piotto, G., Bedin, L. R., & Damasso, M. 2011, A&A, 527, A85
Nascimbeni, V., Cunial, A., Murabito, S., et al. 2013, A&A, 549, A30
Nascimbeni, V., Piotto, G., Börner, A., et al. 2022, A&A, 658, A31
Nelson, B., Ford, E. B., & Payne, M. J. 2014, ApJS, 210, 11
Neveu-VanMalle, M., Queloz, D., Anderson, D. R., et al. 2016, A&A, 586, A93
Newville, M., Stensitzki, T., Allen, D. B., & Ingargiola, A. 2014, https://doi.org/10.5281/zenodo.11813
Öberg, K. I., Murray-Clay, R., & Bergin, E. A. 2011, ApJ, 743, L16
Oshagh, M., Santos, N. C., Boisse, I., et al. 2013, A&A, 556, A19
Parviainen, H., Pallé, E., Nortmann, L., et al. 2016, A&A, 585, A114
Petigura, E. A., Benneke, B., Batygin, K., et al. 2018, AJ, 156, 89
Poddaný, S., Brát, L., & Pejcha, O. 2010, New A, 15, 297
Rauer, H., Catala, C., Aerts, C., et al. 2014, Exp. Astron., 38, 249
Ricker, G. R., Winn, J. N., Vanderspek, R., et al. 2015, J. Astron. Telesc. Instrum. Syst., 1, 014003
Sanchis-Ojeda, R., Winn, J. N., Dai, F., et al. 2015, ApJ, 812, L11
Sha, L., Vanderburg, A. M., Huang, C. X., et al. 2022, MNRAS, submitted [arXiv:2209.14396]
Sinukoff, E., Howard, A. W., Petigura, E. A., et al. 2017, AJ, 153, 70
Steffen, J. H., Ragozzine, D., Fabrycky, D. C., et al. 2012, PNAS, 109, 7982
Taylor, M. B. 2005, ASP Conf. Ser. 347, 29
Taylor, M. B. 2006, ASP Conf. Ser. 351, 666
ter Braak, C. J. F., & Vrugt, J. A. 2008, Stat. Comput., 18, 435
Tinetti, G., Drossart, P., Eccleston, P., et al. 2018, Exp. Astron., 46, 135
Tinetti, G., Eccleston, P., Haswell, C., et al. 2021, ArXiv e-prints [arXiv:2104.04824]
Vanderburg, A., & Johnson, J. A. 2014, PASP, 126, 948
Vanderburg, A., Becker, J. C., Buchhave, L. A., et al. 2017, AJ, 154, 237
Weiss, L. M., Deck, K. M., Sinukoff, E., et al. 2017, AJ, 153, 265
Wenger, M., Ochsenbein, F., Egret, D., et al. 2000, A&AS, 143, 9
Wilson, T. G., Goffo, E., Alibert, Y., et al. 2022, MNRAS, 511, 1043
Zeng, L., Jacobsen, S. B., Sasselov, D. D., et al. 2019, PNAS, 116, 9723
Zerbi, R. M., Chincarini, G., Ghisellini, G., et al. 2001, Astron. Nachr., 322, 275
Zhu, W., Dai, F., & Masuda, K. 2018, RNAAS, 2, 160
Zingales, T., Tinetti, G., Pillitteri, I., et al. 2018, Exp. Astron., 46, 67

1 INAF, Osservatorio Astronomico di Padova, Vicolo dell'Osservatorio 5, 35122 Padova, Italy
   e-mail: valerio.nascimbeni@inaf.it
2 Dipartimento di Fisica e Astronomia "Galileo Galilei", Universita degli Studi di Padova, Vicolo dell'Osservatorio 3, 35122 Padova, Italy
3 INAF, Osservatorio Astrofisico di Catania, Via S. Sofia 78, 95123 Catania, Italy
4 Observatoire Astronomique de l'Université de Genève, Chemin Pegasi 51, 1290 Versoix, Switzerland
5 Physikalisches Institut, University of Bern, Sidlerstrasse 5, 3012 Bern, Switzerland
6 Center for Space and Habitability, University of Bern, Gesellschaftsstrasse 6, 3012 Bern, Switzerland
7 Centre Vie dans l'Univers, Faculté des sciences, Université de Genève, Quai Ernest-Ansermet 30, 1211 Genève 4, Switzerland
8 Aix-Marseille Univ., CNRS, CNES, LAM, 38 rue Frédéric Joliot-Curie, 13388 Marseille, France
9 Centro di Ateneo di Studi e Attività Spaziali "Giuseppe Colombo" (CISAS), Università degli Studi di Padova, Via Venezia 15, 35131 Padova, Italy
10 Instituto de Astrofisica e Ciencias do Espaco, Universidade do Porto, CAUP, Rua das Estrelas, 4150-762 Porto, Portugal
11 Centre for Exoplanet Science, SUPA School of Physics and Astronomy, University of St Andrews, North Haugh, St Andrews KY16 9SS, UK
12 Space sciences, Technologies and Astrophysics Research (STAR) Institute, Université de Liège, Allée du 6 Août 19C, 4000 Liège, Belgium
13 Space Research Institute, Austrian Academy of Sciences, Schmiedlstrasse 6, 8042 Graz, Austria
14 Division of Astrophysics, Department of Physics, Lund University, Box 43, 221 00 Lund, Sweden
15 Astrobiology Research Unit, Université de Liège, Allée du 6 Août 19C, B-4000 Liège, Belgium
16 Instituto de Astrofisica de Canarias, C/ Vía Láctea, s/n, 38200 La Laguna, Tenerife, Spain
17 Departamento de Astrofisica, Universidad de La Laguna, 38206 La Laguna, Tenerife, Spain
18 Institut de Ciencies de l'Espai (ICE, CSIC), Campus UAB, Can Magrans s/n, 08193 Bellaterra, Spain
19 Institut d'Estudis Espacials de Catalunya (IEEC), Carrer del Gran Capità, 2, 08034 Barcelona, Spain
20 Admatis, 5. Kandó Kálmán Street, 3534 Miskolc, Hungary
21 Depto. de Astrofisica, Centro de Astrobiologia (CSIC-INTA), ESAC campus, 28692 Villanueva de la Cañada (Madrid), Spain
22 Departamento de Fisica e Astronomia, Faculdade de Ciencias, Universidade do Porto, Rua do Campo Alegre, 4169-007 Porto, Portugal
23 Université Grenoble Alpes, CNRS, IPAG, CS 40700, 38000 Grenoble, France
24 Department of Astronomy, Stockholm University, AlbaNova University Center, 10691 Stockholm, Sweden
25 Institute of Planetary Research, German Aerospace Center (DLR), Rutherfordstrasse 2, 12489 Berlin, Germany
26 Université de Paris, Institut de physique du globe de Paris, CNRS, 1 rue Jussieu, 75005 Paris, France
27 INAF, Osservatorio Astrofisico di Torino, Via Osservatorio, 20, 10025 Pino Torinese To, Italy
28 Centre for Mathematical Sciences, Lund University, Box 118, 221 00 Lund, Sweden
29 Leiden Observatory, University of Leiden, PO Box 9513, 2300 RA Leiden, The Netherlands
30 Department of Space, Earth and Environment, Chalmers University of Technology, Onsala Space Observatory, 439 92 Onsala, Sweden
31 Dipartimento di Fisica, Universita degli Studi di Torino, via Pietro Giuria 1, 10125, Torino, Italy

[32] University of Vienna, Department of Astrophysics, Türkenschanzstrasse 17, 1180 Vienna, Austria

[33] Science and Operations Department – Science Division (SCI-SC), Directorate of Science, European Space Agency (ESA), European Space Research and Technology Centre (ESTEC), Keplerlaan 1, 2201-AZ Noordwijk, The Netherlands

[34] Konkoly Observatory, Research Centre for Astronomy and Earth Sciences, Konkoly Thege Miklós út 15–17, 1121 Budapest, Hungary

[35] ELTE Eötvös Loránd University, Institute of Physics, Pázmány Péter sétány 1/A, 1117 Budapest, Hungary

[36] IMCCE, UMR8028 CNRS, Observatoire de Paris, PSL Univ., Sorbonne Univ., 77 av. Denfert-Rochereau, 75014 Paris, France

[37] Institut d'astrophysique de Paris, UMR7095 CNRS, Université Pierre et Marie Curie, 98bis blvd. Arago, 75014 Paris, France

[38] Instituto de Astrofísica de Andalucía, Consejo Superior de Investigaciones Científicas, Gta. de la Astronomía, s/n, 18008 Granada, Spain

[39] Department of Astronomy and Astrophysics, University of Chicago, Chicago, IL 60637, USA

[40] Astrophysics Group, Keele University, Staffordshire, ST5 5BG, UK

[41] Department of Astrophysics, University of Vienna, Tuerkenschanzstrasse 17, 1180 Vienna, Austria

[42] Institute of Optical Sensor Systems, German Aerospace Center (DLR), Rutherfordstrasse 2, 12489 Berlin, Germany

[43] Department of Physics, University of Warwick, Gibbet Hill Road, Coventry CV4 7AL, UK

[44] ETH Zurich, Department of Physics, Wolfgang-Pauli-Strasse 2, 8093 Zurich, Switzerland

[45] Cavendish Laboratory, JJ Thomson Avenue, Cambridge CB3 0HE, UK

[46] ESTEC, European Space Agency, 2201AZ, Noordwijk, The Netherlands

[47] Zentrum für Astronomie und Astrophysik, Technische Universität Berlin, Hardenbergstr. 36, 10623 Berlin, Germany

[48] Institut für Geologische Wissenschaften, Freie Universität Berlin, Malteserstraße 74-100, 12249 Berlin, Germany

[49] ELTE Eötvös Loránd University, Gothard Astrophysical Observatory, Szent Imre h. u. 112, 9700 Szombathely, Hungary

[50] MTA-ELTE Exoplanet Research Group, Szent Imre h. u. 112, 9700 Szombathely, Hungary

[51] Institute of Astronomy, University of Cambridge, Madingley Road, Cambridge CB3 0HA, UK

[52] Lund Observatory, Dept. of Astronomy and Theoretical Physics, Lund University, Box 43, 22100 Lund, Sweden

Appendix A: Data tables

Transits of planets WASP-47b, WASP-47d, WASP-47e fitted in the present work (Sect. 3.1) and included in our global dynamical analysis (Section 3.2).

Table A.1. Transits of planet WASP-47b from space-based telescopes included in our global analysis.

source (+ band)	UT date (of T_0)	N	cadence (s)	σ_{phot} (ppm)	T_0 (BJD$_{TDB}$)	$\sigma(T_0)$ (days)	$\sigma(T_0)$ (s)
CHEOPS	2020-06-24	242	60	1050	2459025.11931	0.00054	47
CHEOPS	2020-07-07	251	60	1960	2459037.59764	0.00048	42
CHEOPS	2020-10-02	283	60	1190	2459124.93989	0.00031	26
CHEOPS	2021-07-20	271	60	1130	2459416.08220	0.00083	72
CHEOPS	2021-07-28	236	60	1140	2459424.39829	0.00053	46
CHEOPS	2021-08-18	522	60	1270	2459445.19505	0.00033	29
CHEOPS	2021-08-27	537	60	1140	2459453.51274	0.00038	33
CHEOPS	2021-09-12	357	60	1220	2459470.14844	0.00035	30
CHEOPS	2021-09-16	512	60	1390	2459474.30828	0.00034	29
CHEOPS	2021-09-25	247	60	2630	2459482.62705	0.00085	73
TESS	2021-08-22	412	120	2150	2459449.35394	0.00079	68
TESS	2021-08-27	411	120	3900	2459453.51314	0.00132	114
TESS	2021-08-31	319	120	3330	2459457.66953	0.00107	93
TESS	2021-09-04	412	120	2040	2459461.83102	0.00080	69
TESS	2021-09-08	411	120	2040	2459465.98830	0.00076	66
TESS	2021-09-12	412	120	2110	2459470.14753	0.00083	72
K2	2014-11-21	741	60	347	2456982.97692	0.00043	37
K2	2014-11-25	754	60	342	2456987.13597	0.00008	7
K2	2014-11-29	821	60	357	2456991.29538	0.00008	7
K2	2014-12-03	732	60	342	2456995.45461	0.00022	19
K2	2014-12-08	740	60	349	2456999.61388	0.00009	8
K2	2014-12-12	833	60	348	2457003.77342	0.00008	7
K2	2014-12-16	739	60	352	2457007.93265	0.00008	7
K2	2014-12-20	709	60	354	2457012.09155	0.00043	37
K2	2014-12-24	709	60	362	2457016.25091	0.00008	7
K2	2014-12-28	828	60	354	2457020.40989	0.00008	7
K2	2015-01-02	449	60	361	2457024.56863	0.00037	32
K2	2015-01-06	728	60	361	2457028.72772	0.00008	7
K2	2015-01-10	729	60	362	2457032.88682	0.00008	7
K2	2015-01-14	860	60	346	2457037.04569	0.00008	7
K2	2015-01-18	741	60	352	2457041.20502	0.00008	7
K2	2015-01-22	739	60	345	2457045.36340	0.00041	36

Notes. The columns give the instrument name, the UT date closest to the transit center T_0, the number of photometric data points, the average cadence of the light curve in seconds, the scatter of the residuals from our best-fit model in parts per million, the transit time T_0 in the BJD$_{TDB}$ standard and its associated error, and the latter converted into seconds. The fitting procedure is described in detail in Section 3.1.

Table A.2. Transits of planet WASP-47b from ground-based telescopes included in our global analysis.

source (+ band)	UT date (of T_0)	N	cadence (s)	σ_{phot} (ppm)	T_0 (BJD$_{\mathrm{TDB}}$)	$\sigma(T_0)$ (days)	$\sigma(T_0)$ (s)
REM (g')	2021-09-25	137	60	3002	2459482.61821	0.00197	171
REM (r')	2021-09-25	139	60	2119	2459482.62461	0.00106	91
REM (i')	2021-09-25	139	60	2672	2459482.62212	0.00145	125
ETD (R)	2020-08-30	145	60	1315	2459091.66670	0.00064	56
ETD (R)	2021-07-12	144	60	1581	2459407.76213	0.00082	71
ETD (R)	2021-08-06	141	60	1658	2459432.71923	0.00081	70
ETD (R)	2021-08-31	155	60	1617	2459457.67291	0.00077	67
ETD (R)	2021-09-25	147	60	1540	2459482.62786	0.00073	63
ETD (clear)	2021-09-25	142	60	1723	2459482.62868	0.00084	72
ETD (R)	2021-10-20	129	60	1730	2459507.58050	0.00085	74

Notes. The columns give the instrument name and pass band, the UT date closest to the transit center T_0, the number of photometric data points, the average cadence of the light curve in seconds, the scatter of the residuals from our best-fit model in parts per million, the transit time T_0 in the BJD$_{\mathrm{TDB}}$ standard and its associated error, and the latter converted into seconds. The fitting procedure is described in detail in Section 3.1.

Table A.3. Transits of planet WASP-47d included in our global analysis.

source (+ band)	UT date (of T_0)	N	cadence (s)	σ_{phot} (ppm)	T_0 (BJD$_{\mathrm{TDB}}$)	$\sigma(T_0)$ (days)	$\sigma(T_0)$ (s)
CHEOPS	2020-06-24	242	60	1050	2459025.11931	0.00054	47
K2	2014-11-21	741	60	347	2456982.97692	0.00043	37
K2	2014-11-25	754	60	342	2456987.13597	0.00008	7
K2	2014-11-29	821	60	357	2456991.29538	0.00008	7
K2	2014-12-03	732	60	342	2456995.45461	0.00022	19
K2	2014-12-08	740	60	349	2456999.61388	0.00009	8
K2	2014-12-12	833	60	348	2457003.77342	0.00008	7
K2	2014-12-16	739	60	352	2457007.93265	0.00008	7
K2	2014-12-20	709	60	354	2457012.09155	0.00043	37
K2	2014-12-24	709	60	362	2457016.25091	0.00008	7
K2	2014-12-28	828	60	354	2457020.40989	0.00008	7
K2	2015-01-02	449	60	361	2457024.56863	0.00037	32

Notes. The columns give the instrument name, the UT date closest to the transit center T_0, the number of photometric data points, the average cadence of the light curve in seconds, the scatter of the residuals from our best-fit model in parts per million, the transit time T_0 in the BJD$_{\mathrm{TDB}}$ standard and its associated error, and the latter converted into seconds. The fitting procedure is described in detail in Section 3.1.

Table A.4. CHEOPS data sets used in our analysis.

CH_PR100025_TG005601_V0200	CH_PR100025_TG005602_V0200	CH_PR100017_TG000101_V0200
CH_PR100025_TG005603_V0200	CH_PR100025_TG006201_V0200	CH_PR100025_TG003601_V0200
CH_PR100025_TG006301_V0200	CH_PR100025_TG006302_V0200	CH_PR100025_TG003602_V0200
CH_PR100025_TG006303_V0200	CH_PR100025_TG003603_V0200	

Table A.5. Transits of planet WASP-47e included in our global analysis, part one.

source (+ band)	UT date (of T_0)	N	cadence (s)	σ_{phot} (ppm)	T_0 (BJD$_{TDB}$)	$\sigma(T_0)$ (days)	$\sigma(T_0)$ (s)
K2	2014-11-18	205	60	254	2456979.75947	0.00304	262
K2	2014-11-19	200	60	264	2456980.54893	0.00257	222
K2	2014-11-19	201	60	224	2456981.35038	0.00332	287
K2	2014-11-20	203	60	246	2456982.12025	0.00384	332
K2	2014-11-21	325	60	252	2456982.92710	0.00318	275
K2	2014-11-22	199	60	252	2456983.71289	0.00270	233
K2	2014-11-23	200	60	253	2456984.50296	0.00505	437
K2	2014-11-23	205	60	250	2456985.29435	0.00330	285
K2	2014-11-24	200	60	228	2456986.08074	0.00329	285
K2	2014-11-25	166	60	266	2456986.85811	0.00602	520
K2	2014-11-26	203	60	273	2456987.65827	0.00467	404
K2	2014-11-26	490	60	254	2456988.45285	0.00316	273
K2	2014-11-27	199	60	255	2456989.24063	0.00251	216
K2	2014-11-28	200	60	279	2456990.02070	0.00245	211
K2	2014-11-29	147	60	240	2456990.82061	0.00474	410
K2	2014-11-30	204	60	234	2456991.60066	0.00448	387
K2	2014-11-30	200	60	260	2456992.40463	0.00489	423
K2	2014-12-01	202	60	274	2456993.18662	0.00362	313
K2	2014-12-02	201	60	261	2456993.97574	0.00593	512
K2	2014-12-03	177	60	263	2456994.75999	0.00508	439
K2	2014-12-04	408	60	239	2456995.56292	0.00331	286
K2	2014-12-04	205	60	241	2456996.34540	0.00296	256
K2	2014-12-05	202	60	262	2456997.14358	0.00266	230
K2	2014-12-06	200	60	259	2456997.92454	0.00275	237
K2	2014-12-07	201	60	247	2456998.71861	0.00327	283
K2	2014-12-08	436	60	250	2456999.51625	0.00350	302
K2	2014-12-08	198	60	246	2457000.29460	0.00373	322
K2	2014-12-09	202	60	254	2457001.08737	0.00246	213
K2	2014-12-10	201	60	236	2457001.87632	0.00405	350
K2	2014-12-11	204	60	281	2457002.66183	0.00265	229
K2	2014-12-11	202	60	244	2457003.45503	0.00373	323
K2	2014-12-12	562	60	271	2457004.25990	0.00611	528
K2	2014-12-13	199	60	283	2457005.03130	0.00306	264
K2	2014-12-14	198	60	249	2457005.81762	0.00296	255
K2	2014-12-15	201	60	234	2457006.60588	0.00432	373
K2	2014-12-15	201	60	253	2457007.39847	0.00258	223
K2	2014-12-16	200	60	259	2457008.19565	0.00477	412
K2	2014-12-17	200	60	254	2457008.98670	0.00362	313
K2	2014-12-18	201	60	230	2457009.76817	0.00270	233
K2	2014-12-19	198	60	267	2457010.55274	0.00578	499
K2	2014-12-19	201	60	257	2457011.34426	0.00246	212
K2	2014-12-20	330	60	252	2457012.13715	0.00429	370
K2	2014-12-21	204	60	255	2457012.93793	0.00681	589

Notes. The columns give the instrument name, the UT date closest to the transit center T_0, the number of photometric data points, the average cadence of the light curve in seconds, the scatter of the residuals from our best-fit model in parts per million, the transit time T_0 in the BJD$_{TDB}$ standard and its associated error, and the latter converted into seconds. The fitting procedure is described in detail in Section 3.1.

Table A.6. Transits of planet WASP-47e included in our global analysis, part two.

source (+ band)	UT date (of T_0)	N	cadence (s)	σ_{phot} (ppm)	T_0 (BJD$_{TDB}$)	$\sigma(T_0)$ (days)	$\sigma(T_0)$ (s)
K2	2014-12-22	202	60	251	2457013.71727	0.00428	370
K2	2014-12-23	203	60	245	2457014.50350	0.00308	266
K2	2014-12-23	437	60	278	2457015.29893	0.00384	331
K2	2014-12-24	483	60	253	2457016.08502	0.00295	255
K2	2014-12-25	201	60	265	2457016.87618	0.00274	237
K2	2014-12-26	200	60	255	2457017.65928	0.00437	377
K2	2014-12-26	200	60	263	2457018.43617	0.00806	696
K2	2014-12-27	199	60	252	2457019.24832	0.00340	294
K2	2014-12-28	202	60	263	2457020.03209	0.00206	178
K2	2014-12-29	202	60	254	2457020.81683	0.00758	654
K2	2014-12-30	202	60	264	2457021.61423	0.00370	320
K2	2014-12-30	203	60	272	2457022.40380	0.00212	183
K2	2014-12-31	201	60	238	2457023.19910	0.00341	294
K2	2015-01-01	204	60	234	2457023.98302	0.00273	236
K2	2015-01-02	203	60	260	2457024.76911	0.00598	517
K2	2015-01-03	197	60	277	2457025.55298	0.00472	407
K2	2015-01-03	201	60	254	2457026.35331	0.00363	314
K2	2015-01-04	201	60	258	2457027.13956	0.00633	547
K2	2015-01-05	202	60	278	2457027.92824	0.00362	313
K2	2015-01-06	574	60	267	2457028.81569	0.00465	402
K2	2015-01-07	426	60	276	2457029.53520	0.00262	226
K2	2015-01-07	199	60	281	2457030.31036	0.00386	334
K2	2015-01-08	200	60	256	2457031.09123	0.00237	205
K2	2015-01-09	202	60	241	2457031.87981	0.00380	329
K2	2015-01-10	705	60	277	2457032.69619	0.00495	427
K2	2015-01-10	360	60	268	2457033.46157	0.00282	243
K2	2015-01-11	199	60	254	2457034.24470	0.00566	489
K2	2015-01-12	194	60	244	2457035.03214	0.00453	391
K2	2015-01-13	180	60	255	2457035.82366	0.00243	210
K2	2015-01-14	204	60	244	2457036.61598	0.00198	171
K2	2015-01-14	200	60	262	2457037.39259	0.00715	618
K2	2015-01-15	200	60	260	2457038.19202	0.00411	355
K2	2015-01-16	202	60	213	2457038.98832	0.00280	242
K2	2015-01-17	170	60	238	2457039.77635	0.00498	430
K2	2015-01-18	201	60	246	2457040.56530	0.00370	320
K2	2015-01-18	471	60	253	2457041.35437	0.00278	240
K2	2015-01-19	202	60	261	2457042.14436	0.00263	227
K2	2015-01-20	199	60	270	2457042.93246	0.00312	270
K2	2015-01-21	169	60	258	2457043.72336	0.00304	263
K2	2015-01-22	199	60	251	2457044.50829	0.00253	218
K2	2015-01-22	365	60	257	2457045.30637	0.00452	390
K2	2015-01-23	203	60	261	2457046.08877	0.00422	365

Notes. The columns give the instrument name, the UT date closest to the transit center T_0, the number of photometric data points, the average cadence of the light curve in seconds, the scatter of the residuals from our best-fit model in parts per million, the transit time T_0 in the BJD$_{TDB}$ standard and its associated error, and the latter converted into seconds. The fitting procedure is described in detail in Section 3.1.